Electrolyte Failure and Reconstruction towards Li–S Batteries Operating from –20 °C to 100 °C

Dong Guo [a], Simil Thomas [a], Jehad K. El-Demellawi [b], Zixiong Shi [a], Zhiming Zhao [a], Christian G. Canlas [c], Yongjiu Lei [a], Jian Yin [a], Yaping Zhang [c], Mohamed Nejib Hedhili [c], Muhammad Arsalan [d], Yunpei Zhu [a], Osman M. Bakr [a], Omar F. Mohammed [a], Husam N. Alshareef *[a]

[a] Center for Renewable Energy and Storage Technologies (CREST), Physical Sciences and Engineering Division, King Abdullah University of Science and Technology (KAUST), Thuwal 2319955-6900, Saudi Arabia. E-mail: husam.alshareef@kaust.edu.sa

[b] KAUST Upstream Research Center (KURC), EXPEC-ARC, Saudi Aramco, Thuwal, 23955-6900, Saudi Arabia

[c] Core Labs, King Abdullah University of Science and Technology (KAUST), Thuwal 23955-6900, Saudi Arabia

[d] EXPEC Advanced Research Center, Saudi Aramco, P.O. Box 5000, Dhahran 31311, Saudi Arabia

Experimental section

Preparation of electrolytes: The solvent, Tris(2,2,2-trifluoroethyl)phosphate (TFEP, 99.8%), Tetraethylene glycol dimethyl ether (TEGDME, 99.8%), Triethyl phosphate (TEP, 99.8%) were obtained from DoDoChem. 1,3-Bis(1,1,2,2-tetrafluoroethoxy)propane (BTFP, 99%) was ordered from Zhengzhou Alfa Chemical Co., Ltd. All the solvents were dried with 4 Å molecular sieves for at least 24h before electrolyte preparation. 1 M Lithium bis(trifluoromethane)sulfonimide (LiTFSI, Solvionic Corporation) in TFEP was prepared by dissolving 1mmol LiTFSI in 1ml TFEP in the glovebox, and the other electrolytes with different solvents and salt concentrations were prepared with the same procedure.

Preparation of the cathode: Elemental sulfur (Sigma-Adrich) and polyacrylonitrile (Sigma-Aldrich, M_w = 150 000) were mixed at a weight ratio of 4:1 and grinded before being heated at 450 °C for 6 h in an argon-flowing tube furnace. The pristine SPAN powder could be obtained after cooling to room temperature. To further exclude the residual elemental sulfur, the as-obtained SPAN powder was treated by Soxhlet extraction for 24h using toluene as the solvent. Purified SPAN samples were then vacuum dried at 100 °C overnight. Afterward, the SPAN, Super-P, multi-walled carbon nanotubes (XFM01, XFNANO Materials Tech Co., Ltd.), and sodium carboxymethyl cellulose (CMC) binder were well mixed with a mass ratio of 7:1:1:1 with ultra-pure water as solvent. The slurry was then blading cast on carbon-coated Al foil, followed by vacuum drying at 80 °C overnight. The obtained cathode has a controlled mass loading of ~2 mg cm^{-2} for coin cell assembly.

Assembly of Li-SPAN pouch cells. All pouch cells were fabricated using lithium metal anodes and the prepared SPAN cathodes and electrolytes. The dimensions of the cathode and anode are

52*59.5 and 54*61.5 mm^2, respectively. The thickness of the Li metal anode at each side is around 100 μm. Each pouch cell was assembled by sequentially stacking the cathode, separator (100 μm), and Li anode foil on each other and finally sealed with an Al plastic film package. The sulfur loading in the cathode for all the pouch cells was around 7 mg cm^{-2} (double-side coated). During the fabrication and formation process, a pressure of 0.12 MPa was applied to the pouch cells to ensure the desired interfacial contact between the separator and electrodes. The pouch cells were assembled in a dry room with the dew point controlled at around -45 °C.

Characterizations: The structures of the as-prepared electrolytes were analyzed by ^{1}H, ^{7}Li, ^{19}F nuclear magnetic resonance (NMR) spectroscopy using a Bruker Avance III 600 MHz NMR spectrometer equipped with a BBFO probe and temperature controller. A coaxial insert with 0.1 M LiPF$_6$ salt dissolved in the deteriorated dimethyl sulfoxide (DMSO-d$_6$) was applied as the reference to ensure the accuracy of the NMR test. Dry N$_2$ was employed for sample spinning to prevent samples from degradation. All electrolytes were characterized using two-dimensional (2D) diffusion-ordered spectroscopy (DOSY). ^{7}Li DOSY was conducted with 16 scans per increment, 3 ms gradient length, and 125 ms diffusion delay. The quantified NMR for the electrolyte retention analysis is conducted following previously reported similar procedures.[1]

The room temperature and high-temperature 2D ^{1}H-^{19}F heteronuclear Overhauser NMR spectroscopy (HOESY) experiments were obtained on a 600 MHz Bruker AVANCE III NMR spectrometer equipped with a BBFO probe. The T$_1$ relaxation times of ^{1}H and ^{19}F at both temperatures were measured using the inversion recovery method. The ^{1}H-^{19}F HOESY experiment with non-gradient QNP-operation was conducted using a ^{19}F 90-degree pulse ranging from 14-17 us, ^{1}H 90-degree pulse of 11 us, mixing times from 0.6-2.5s and 112-160 scans.

The room temperature and high-temperature 2D ^{19}F-^{7}Li solution-state HOESY experiments were obtained on a 900 MHz Bruker AVANCE III wide-bore NMR spectrometer equipped with a 3.2mm H/F-X CPMAS probe. The T_1 relaxation times of the ^{7}Li and ^{19}F nuclei at both temperatures were measured using the inversion recovery method. The ^{19}F - ^{7}Li phase-sensitive HOESY experiment was conducted using a ^{7}Li 90-degree pulse of 12 us, ^{19}F 90-degree pulse of 11 us, mixing times from 0.35 to 0.8s, and 112 scans.

XPS analysis was performed with a Kratos analytical spectrometer at room temperature with monochromatic Al Kα (1,486.6 eV) radiation. To avoid exposure to air, the cells were disassembled inside a glovebox, and the samples were transferred to the XPS chamber through a sealed argon-filled capsule. The adventitious carbon peak at 248.8 eV was used for calibration. For the time-of-flight secondary ion mass spectrometry (TOF-SIMS), 1kev Cs^+ ion beam was applied for the sputtering, and 30 keV Bi^{3+} was applied for the analysis at the negative test mode. The sputtering and analysis areas were 200×200 μm^2 and 50×50 μm^2, respectively. Before the TOF-SIMS and XPS tests, the cycled electrodes were gently washed with fresh DME solvent and dried in an argon-filled glove box. The small-angle X-ray scattering (SAXS) measurements were performed on a Xeuss 3.0 high-resolution X-ray scattering system equipped with a Dectris Eiger2 4M detector and two Genix3D CuKα radiation sources at wavelength λ = 1.542 Å (50kV, 60mA). A silver behenate standard was used for wavevector calibration, and a glassy carbon standard was used for absolute intensity calibration. A 200mm sample-to-detector-distance, high-resolution collimation with 13MPh/s at an empty position (no samples) was applied, and the measuring time was 3 hours for each sample.

Electrochemical measurements: Coin-type (CR2032) cells were assembled inside an Ar-filled glove box with lithium metal as the anode, and glass fiber was used as the separator. The

electrolytes were prepared following the above-mentioned procedures. Galvanostatic charge/discharge was conducted in a fixed voltage range of 1–3 V vs. Li^+/Li on Neware battery test system (CT-4800 5V 50mA, Shenzhen, China). The batteries for high-temperature testing were cycled in the thermal chamber which was connected to the Neware battery tester by thermal-resistant cables. In this work, the specific capacity was calculated based on the mass of SPAN, and the cells were cycled at various C rates (1C = 600 mAh g^{-1}). For the shallow depth of discharge test, the cell was cycled at 100% discharge/charge for one cycle, and then the cycling test was conducted by discharge cutoff voltage at 2.1V and then full charge to 3 V at 100 °C and 0.5C rate. For low temperature testing, the cells were activated at 20 °C by running 5 cycles with 0.2C and then were cycled at low temperatures. For the high temperature cycling, the cells were directly rested in thermal chamber for 4 h and then galvanostatic cycled at 100 °C. For the lean electrolyte test, thermally resistant polyimide (PI) separators (20 μm) were utilized, as it requires a smaller amount of electrolyte for adequate wetting. Electrochemical impedance spectroscopic (EIS), CV, LSV, and chronoamperometry measurements were performed on a VMP3 potentiostat (BioLogic). The reduction and oxidation stability of the electrolytes were investigated by LSV and chronoamperometry test, and a carbon-coated Al foil was used as the working electrode, and lithium metal was used as both the reference and counter electrodes.

Theoretical Calculations.

We performed Ab initio molecular dynamics (AIMD) simulations employing CP2K software.[2] These calculations were performed at the Γ-point only using Perdew-Burke-Ernzerhof (PBE) exchange-correlation function; long-range dispersive interactions were included using the Grimme DFT-D3 method.[3] We have used a plane-wave cut-off of 400 Ry and Goedecker-Teter-Hutter (GTH) pseudopotentials along with DZVP-MOLOPT-SR-GTH basis sets in all the calculations.

We simulated five model aqueous electrolyte systems with the concentration of Li-TFSI and organic solvents to be consistent with experiments. The volume of the computed cubic supercell for each electrolyte was set based on experimental density. The dimension of the cubic unit cell and the total number of atoms for each aqueous electrolyte were summarized as: $a = 21.40$ Å and 931 atoms for 1 M LiTFSI/TEGDME, $a = 21.03$ Å and 834 atoms for 1 M LiTFSI/TEP, $a = 21.20$ Å and 678 atoms for 1 M LiTFSI/TFEP, $a = 22.81$ Å and 838 atoms for 3 M LiTFSI/TFEP, and $a = 23.12$ Å and 946 atoms for 0.7 M LiTFSI/(TFEP:BTFP). Initial configurations were generated using Packmol software and simulations were run for 2.0 ps (20000 steps) in the NVE ensemble, followed by an equilibration step for 40 ps (40000 steps) using the NVT ensemble. A time step of 1.0 fs is used in all the calculations.

Density functional theory (DFT) calculations for the isolated clusters (namely, Highest occupied molecular orbital (HOMO) and lowest unoccupied molecular orbital (LUMO)) were calculated at ωB97X-D/6-31+G** level using the Gaussian 16 (revision C.02) suite of programs.[4]
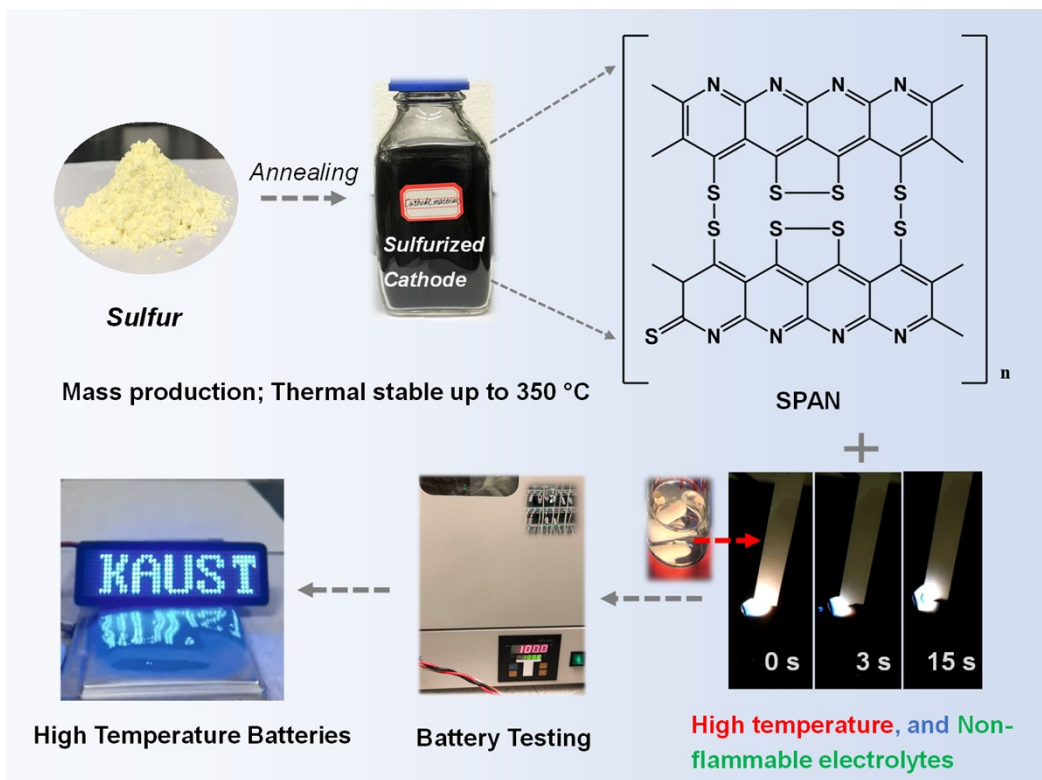
Fig. S1. Schematic illustration of the fabrication process of Li-SPAN cells for extreme temperature environments.
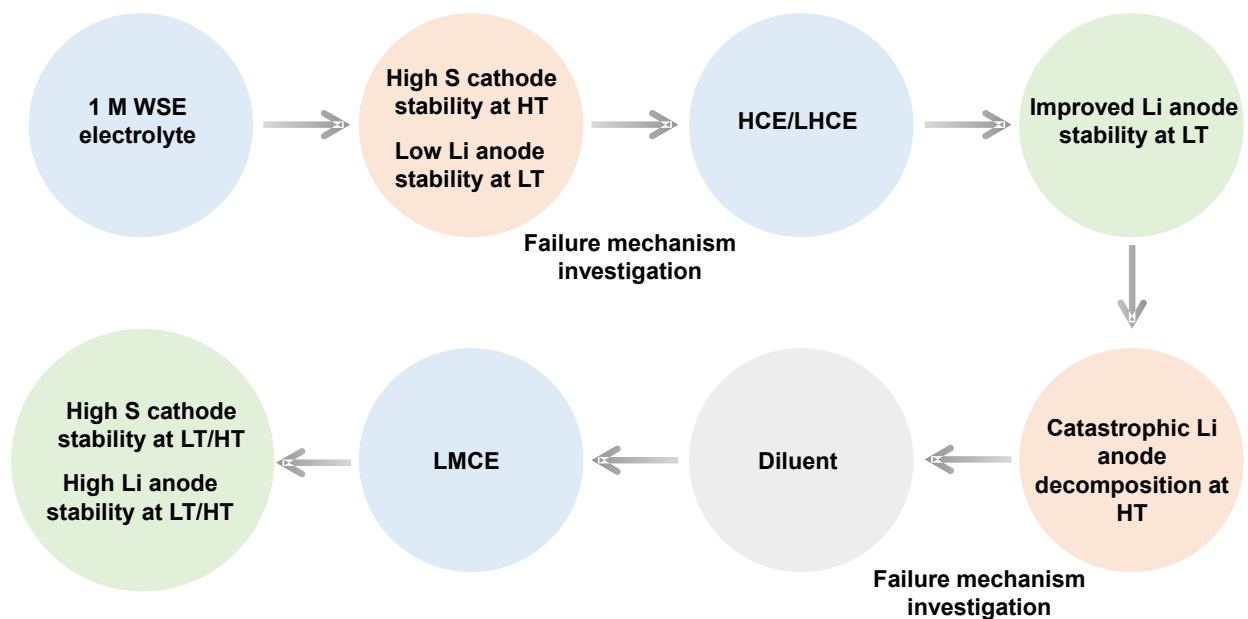
Fig. S2. Design process of LMCE electrolyte for Li-S batteries working at -20 –100 °C.
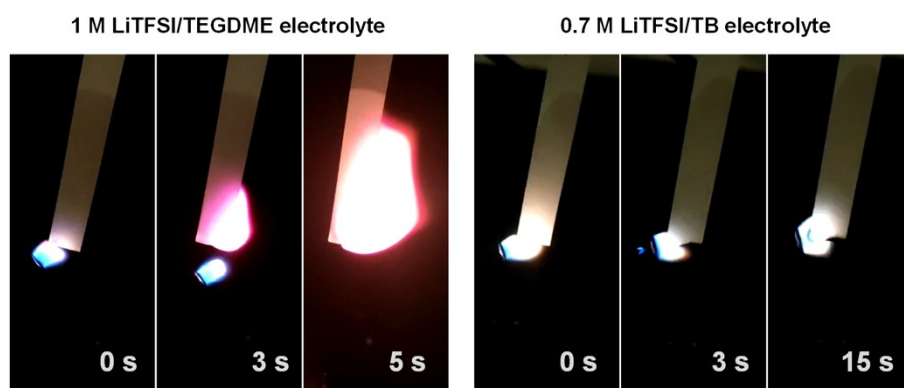
**Fig. S3**. Flammability test of the different electrolytes.
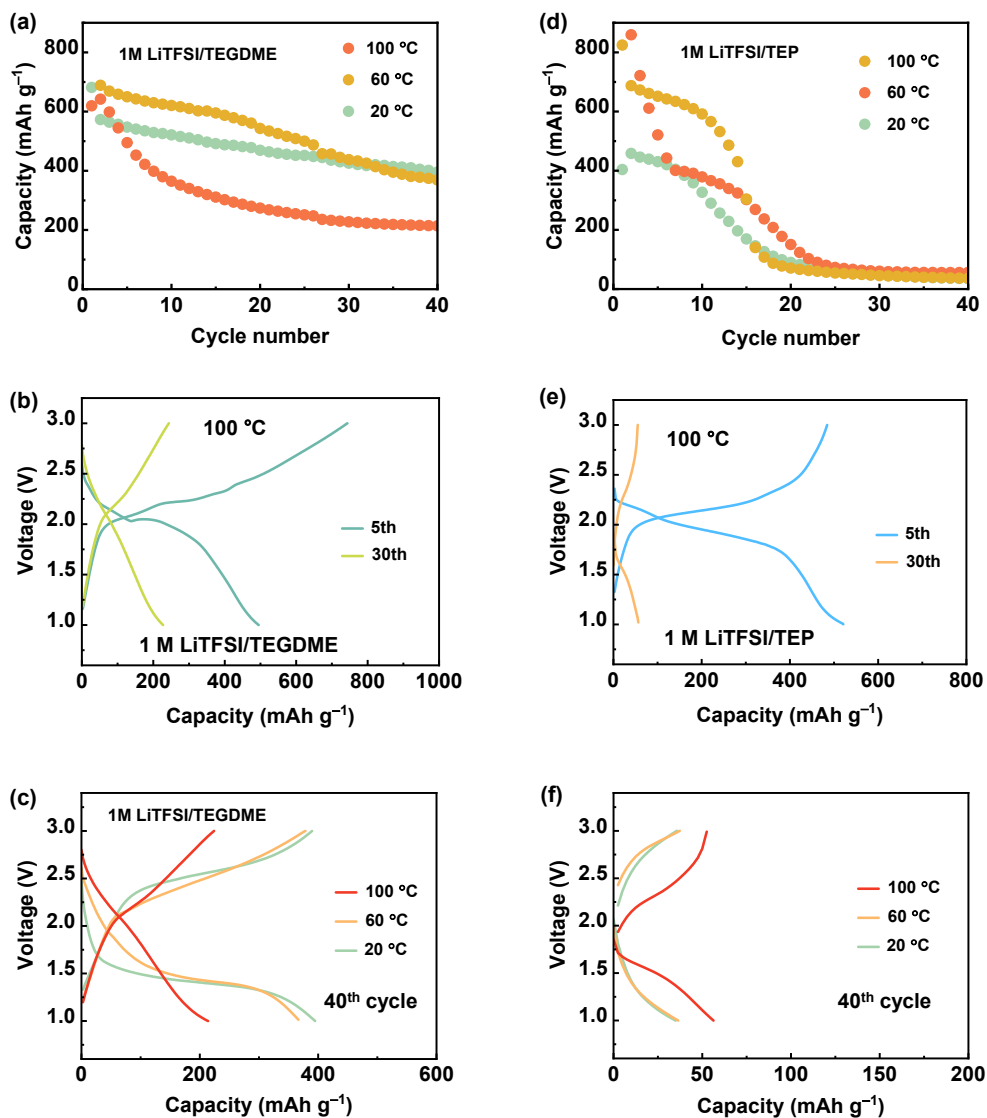
Fig. S4. Electrochemical performance of the Li-SPAN batteries at different temperatures with (a-c) 1 M LiTFSI/TEGDME electrolyte and (d-f) 1 M LiTFSI/TEP electrolyte. For the 1 M LiTFSI/TEGDME electrolyte, the cycling stability of the Li-SPAN cell significantly decreased at higher temperatures, with the stability at 20 > 60 > 100 °C, indicating that the cathode sulfur solubility, which is highly influenced by temperature, has dominated the cycling performance. This is also suggested by discharge-charge plateaus at different temperatures, as shown in Fig. 3b-c. For the 1 M LiTFSI/TEP, the cell degraded fast at both low and high temperatures, indicating that apart from cathode solubility, anode instability also contributed to the inferior cycling performance, as revealed by the performance of Li-Li symmetric cells in Fig. S5.
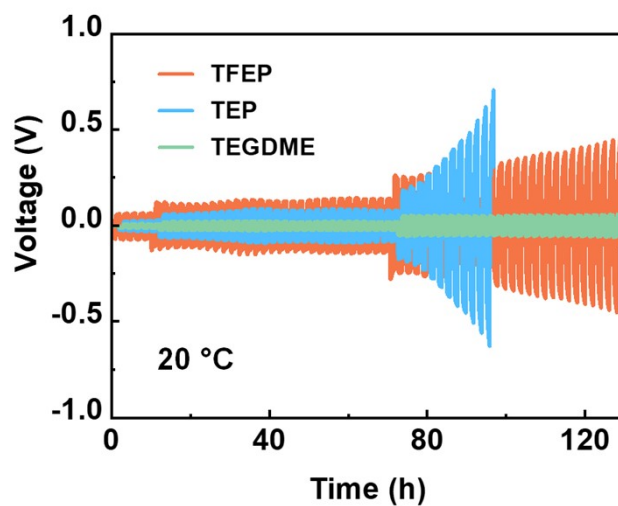
Fig. S5. Voltage profiles of Li-Li symmetric cells fabricated with 1 M LiTFSI in different solvents at 20 °C.
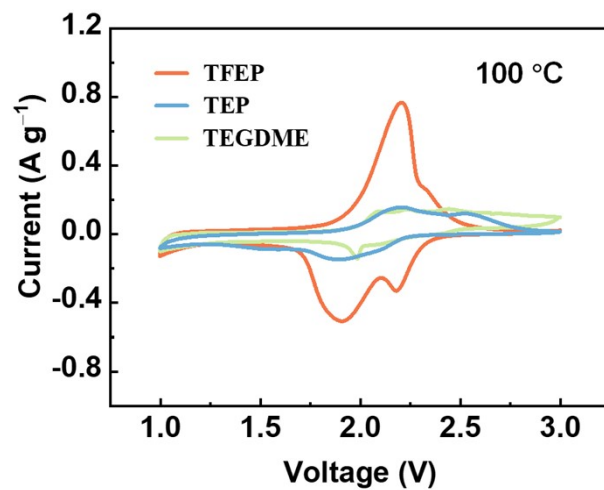
Fig. S6. CV profiles of Li-SPAN cells at 100 °C and a scan rate of 0.1mV s^{-1}. The electrolyte is 1 M LiTFSI in different solvents.
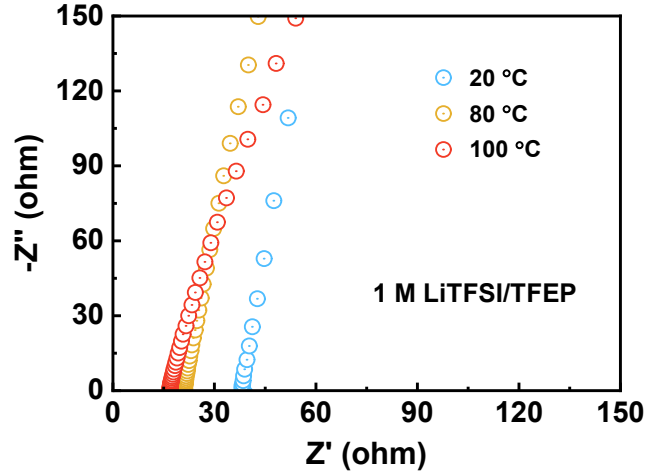
Fig. S7. The electrochemical impedance spectra of SS | SS symmetric cells using 1 M LiTFSI/TFEP electrolyte at different temperatures. The measured resistance values are 38.1 Ω, 21.2 Ω, and 16.8 Ω at 20 °C, 80 °C, and 100 °C, respectively. Using the equation, $\sigma = \dfrac{l}{RS}$, where l represents the thickness of separator, R represents the resistance obtained from EIS measurements, and S represents the area of electrodes, the ionic conductivity was calculated to be 1.7×10^{-4}, 3.06×10^{-4}, and 3.86×10^{-4} S cm^{-1} at 20 °C, 80 °C, and 100 °C, respectively.
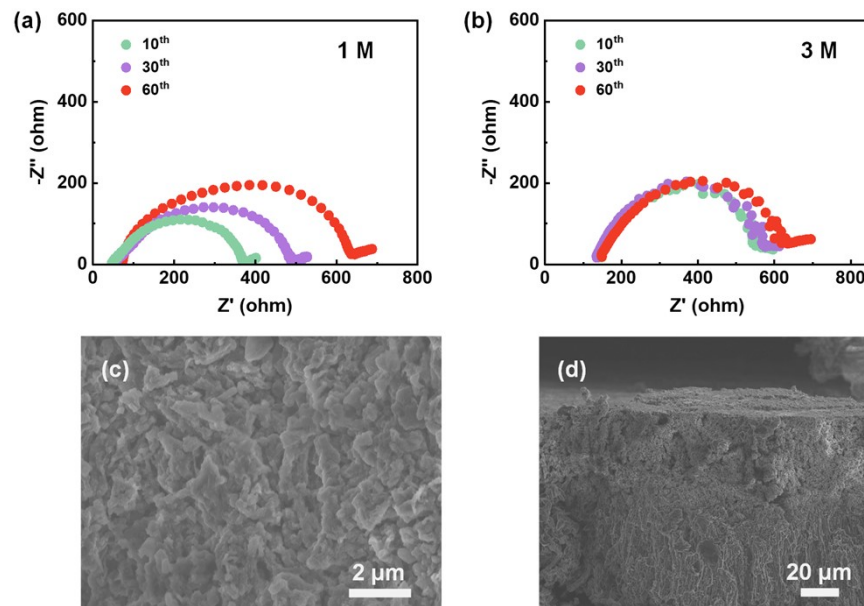
Fig. S8. EIS results for the Li-Li symmetric cells cycling with (a) 1 M LiTFSI/TFEP and (b) 3 M LiTFSI/TFEP electrolyte at 20 °C after different cycles. (c, d) Surface and cross-section images of the Li anode cycling with 1 M LiTFSI/TFEP electrolyte after 60 cycles.

Although the Li-Li cell with 1 M LiTFSI/TFEP electrolyte exhibited lower resistance in the initial cycle compared to the 3 M LiTFSI/TFEP electrolyte, the interfacial resistance increased significantly more in subsequent 60 cycles with the 1 M LiTFSI/TFEP electrolyte. The substantial rise in interfacial impedance indicates that the Li anode is deteriorating in the 1 M electrolyte at 20 °C, and this agrees with the increased Li-Li polarization observed in Fig. 2a. To further confirm this, SEM images of the lithium anode cycled with the 1 M electrolyte were collected after 60 cycles. The cycled lithium anode exhibited a rugged and porous surface, and the cross-sectional images further reveal a highly corroded lithium anode, indicating uneven lithium plating and parasitic reactions, which contributed to poor cycling performance at lower temperatures.
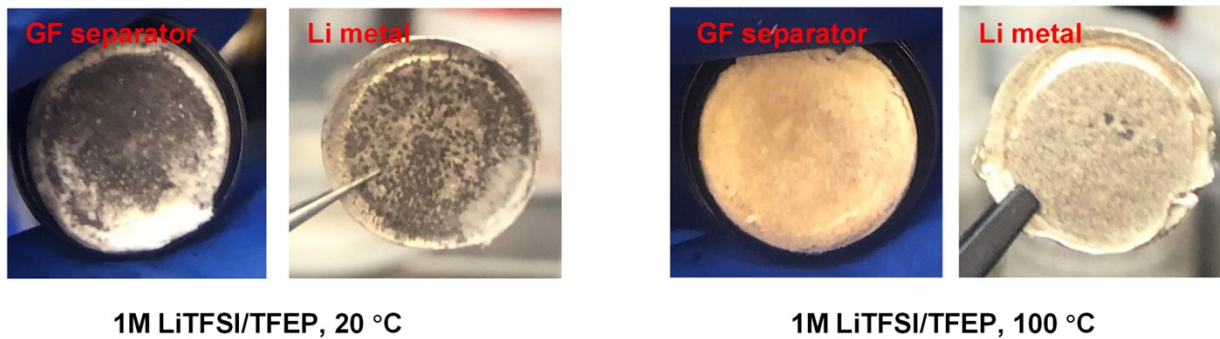
Fig. S9. Digtal photograph of glassfiber separator and lithium metal anode after cycling in Li-Li symmetric cells with 1 M LiTFSI/TFEP electrolyte at 20 °C and 100 °C, respectively.
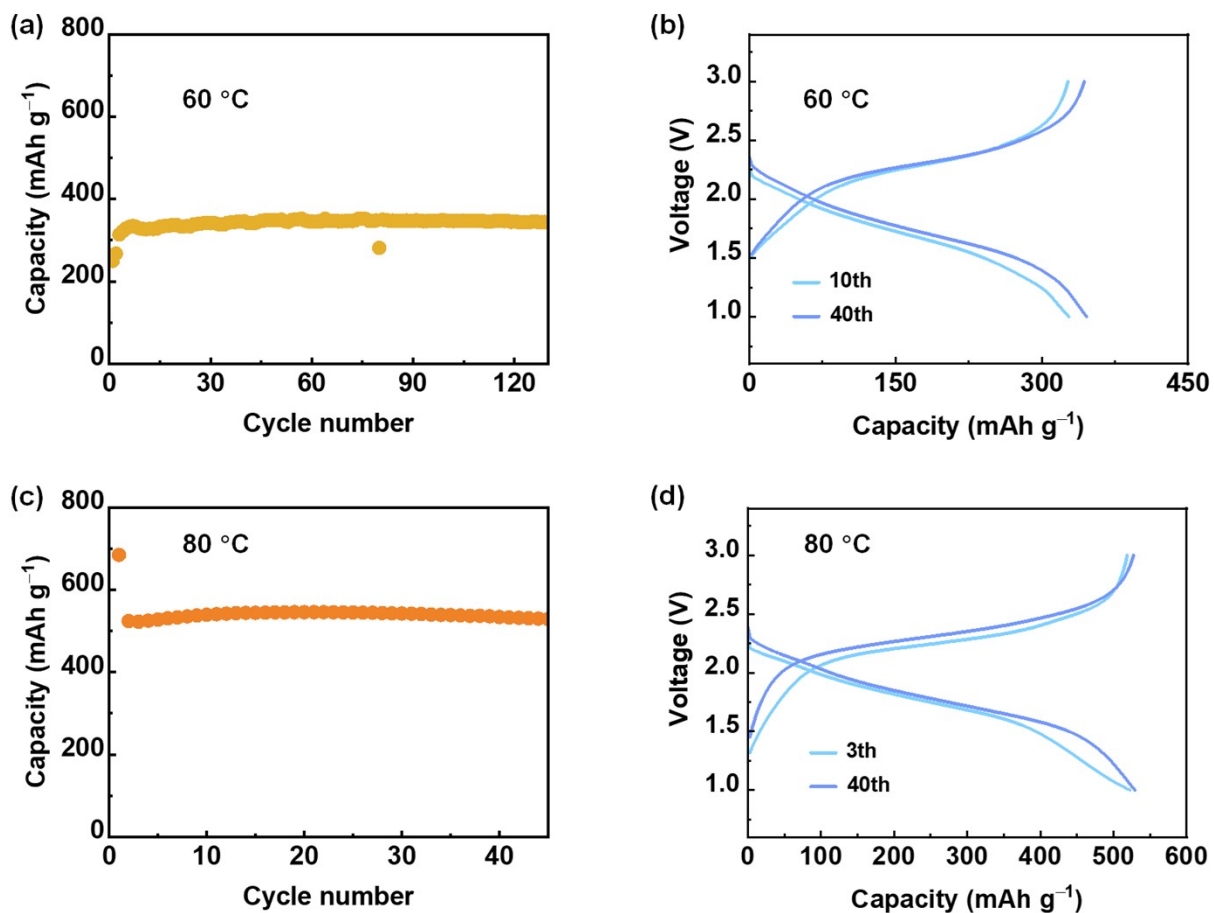
Fig. S10. Cycling performance of 3 M LiTFSI/TFEP electrolyte at moderate temperatures of 60 °C and 80 °C. The abrupt decreased capacity at 77th cycle (a) was due to a temporary temperature fluctuation when the thermal chamber was opened.
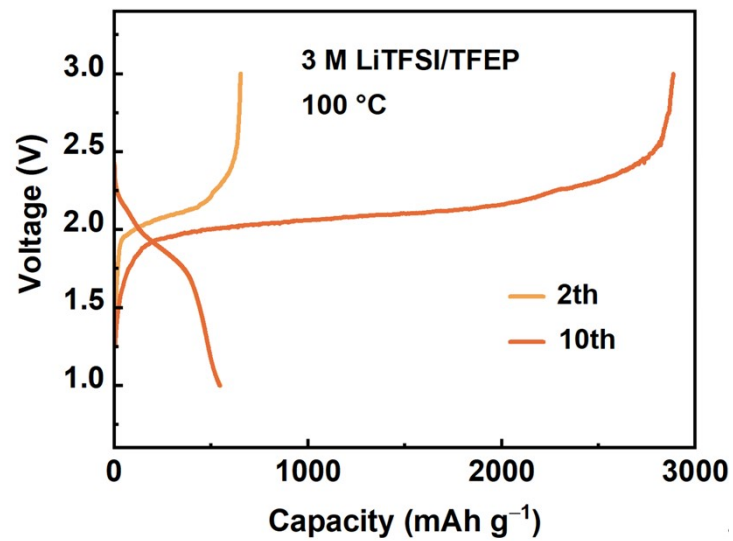
Fig. S11. Discharge-charge profile of Li-SPAN cell with 3 M LiTFSI/TFEP electrolyte at 100 °C.
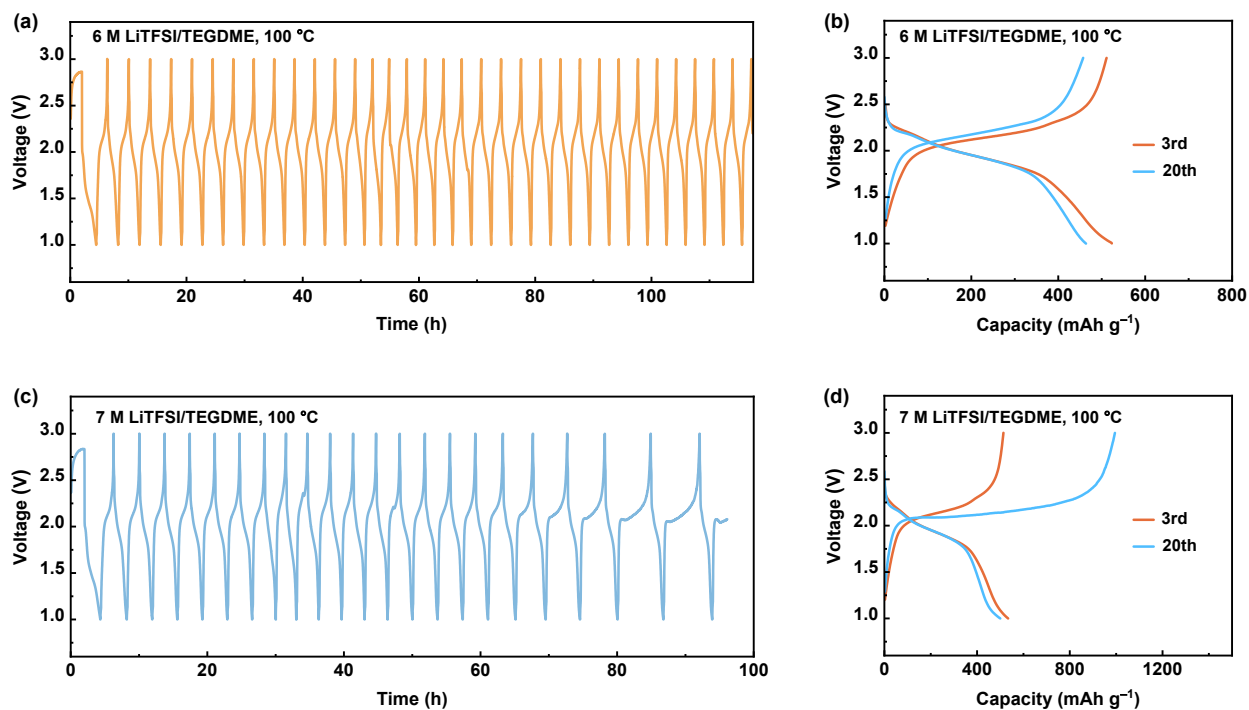
Fig. S12. Cycling performance and discharge-charge profile of Li-SPAN cell with (a-b) 6 M LiTFSI/TEGDME and (c-d) 7 M LiTFSI/TEGDME electrolyte at 100 °C. 7 M is approaching the saturated state of the solution. Note that the charge curve of Li-SPAN is normal with 6 M LiTFSI in TEGDME electrolytes but failed with 7 M eletrolyte. Similar to the TFEP electrolyte, this ether-based electrolyte again confirmed that when electrolyte concentration is high enough, lithium metal batteries fail at an EHT of 100 °C due to the serious parasite decomposition.
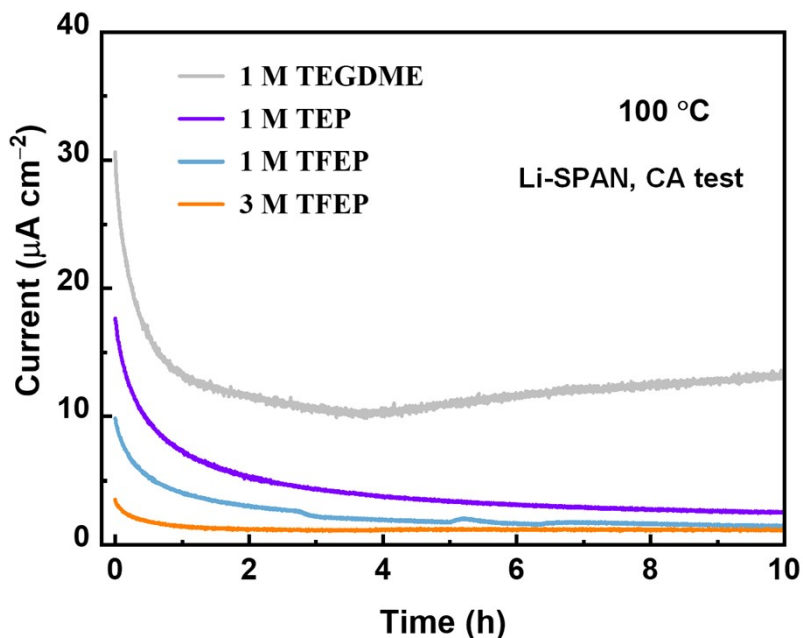
Fig. S13. Chronoamperometry (CA) profiles of the Li-SPAN coin cells at 3 V in different electrolytes at 100 °C.
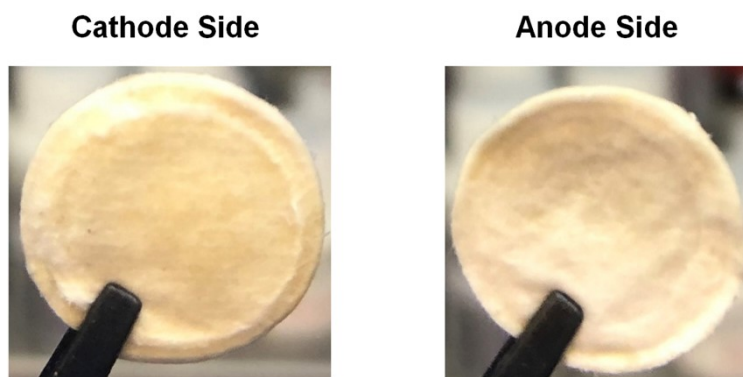
Fig. S14. Digital photographs of the GF separator in Li-SPAN cell after 10 cycles at 100 °C. The electrolyte used was 1 M LiTFSI/TFEP. The separator facing cathode side and anode side showed no apparent black side product, as opposite to the GF separator cycled in 3 M electrolyte.
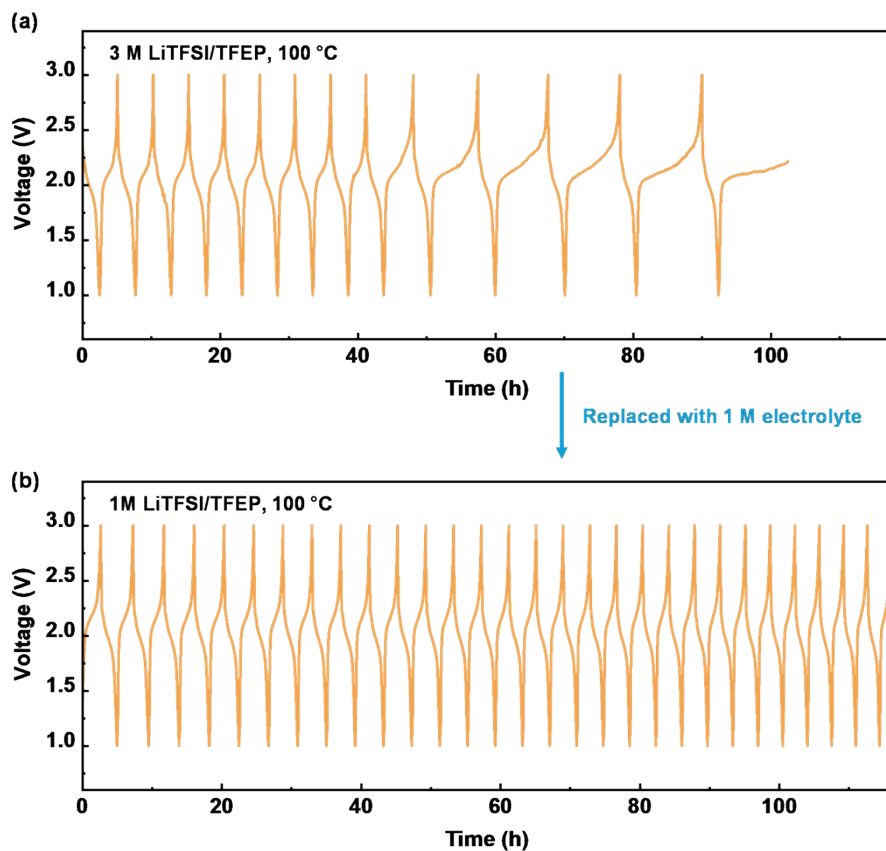
Fig. S15. (a) Voltage profile of Li-SPAN cell with 3 M LiTFSI/TFEP electrolyte at 100 °C. (b) Voltage profile for the cell that was disassembled and refilled with 1 M LiTFSI/TFEP electrolyte.
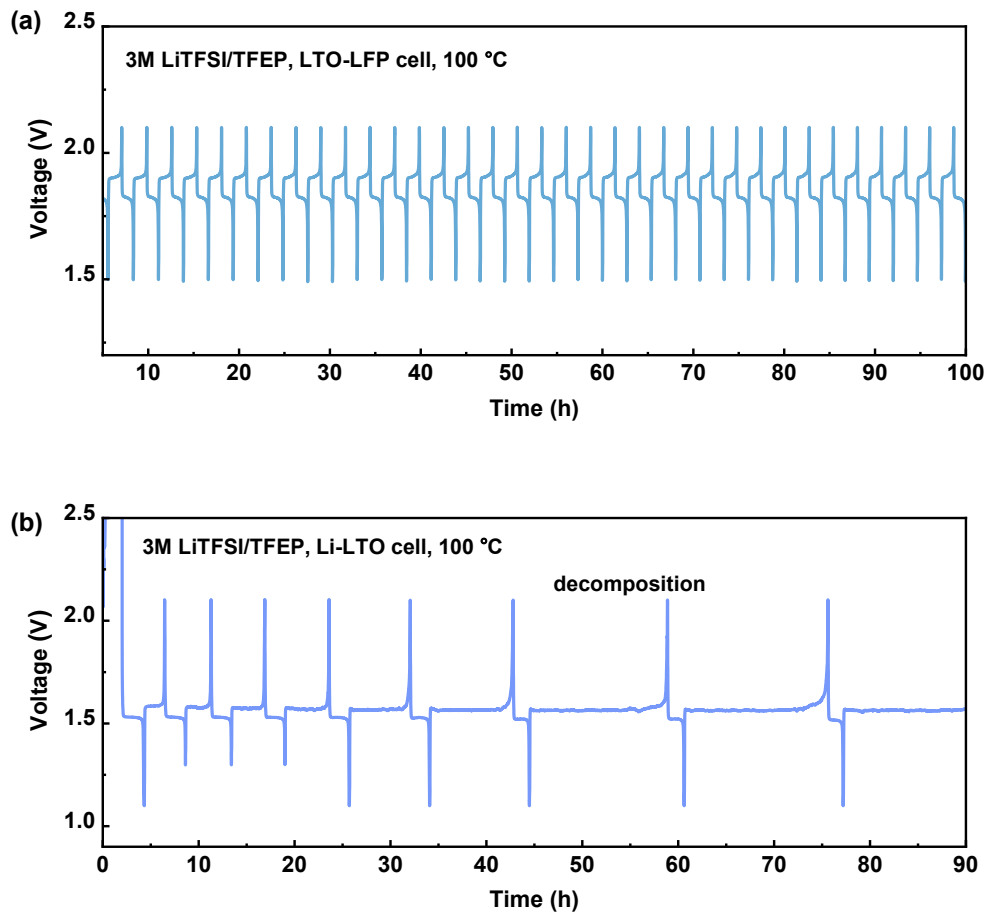
Fig. S16. Voltage profiles for the (a) LTO-LFP cell and (b) Li-LTO cell with 3 M LiTFSI/TFEP electrolyte. The cells were cycled at 100 °C and 0.5 C rate. We note that both LTO and LFP electrodes are highly thermally stable, so the decomposition from electrodes can be excluded.
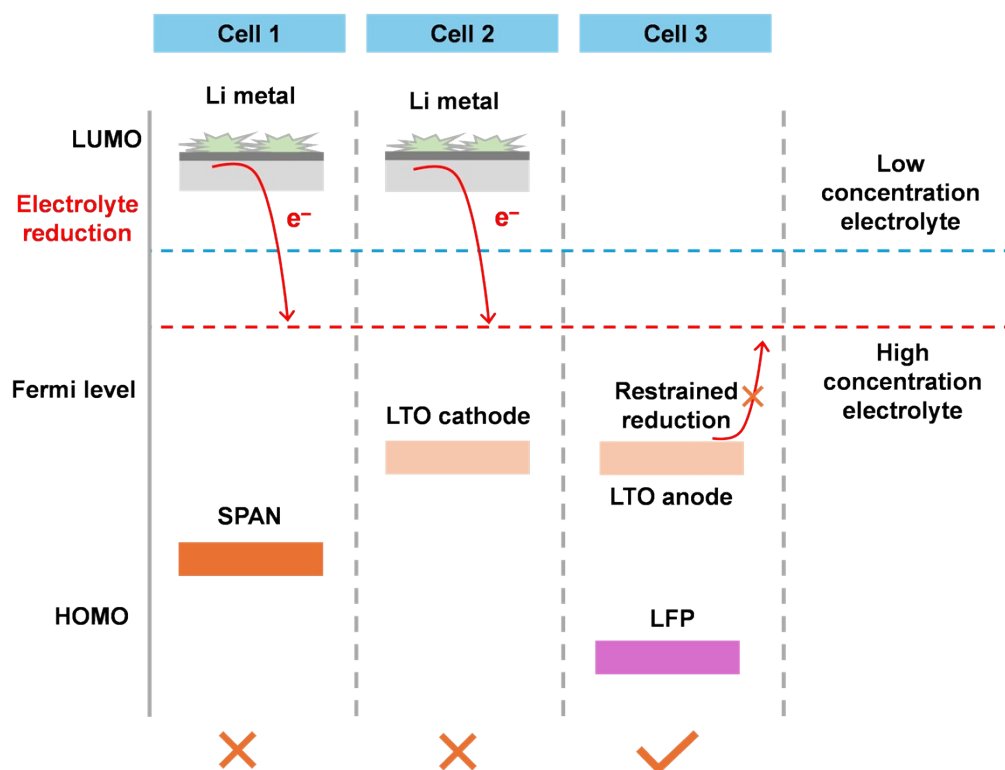
Fig. S17. An illustration of the potential-dependent electrolyte reductive decomposition in various cell systems. Anion aggregates in high-concentration electrolytes have low LUMO levels, thereby are thermodynamically easier to receive electrons from Li metal anode and reduced than that of lower electrolytes. This may cause continuous electrolyte reduction at EHT when the SEI could not protect the interphase. Therefore, cells using Li metal anode such as Li-SPAN and Li-LTO failed, while LTO-LFP worked due to the lower LUMO of LTO as an anode.
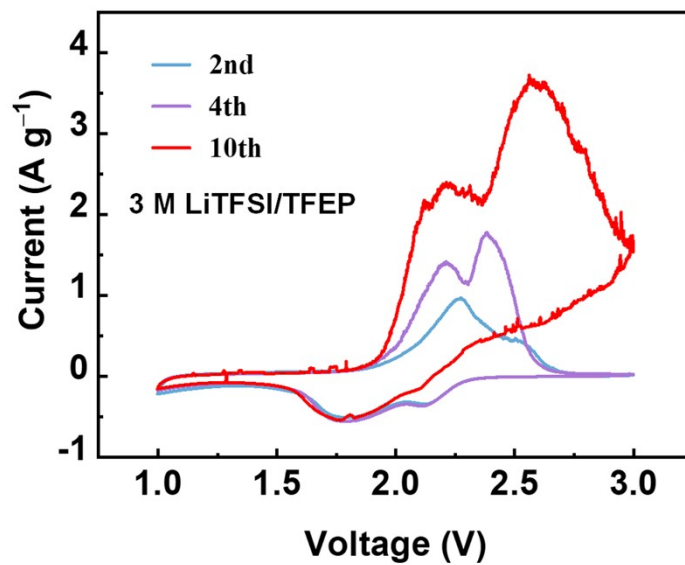
Fig. S18. CV profiles of the Li-SPAN cell cycling with 3 M LiTFSI/TFEP electrolyte at 100 °C.
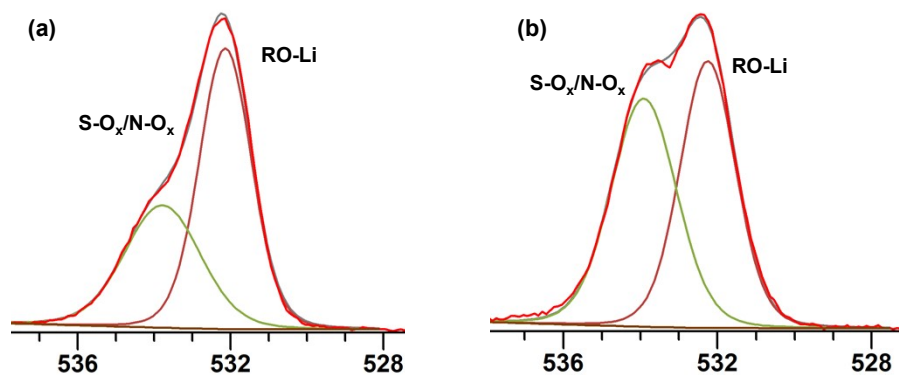
Fig. S19. O1s XPS results for the SPAN cathode after 10 cycles at 100 °C with (a) 1 M LiTFSI/TFEP electrolyte and (b) 3 M LiTFSI/TFEP electrolyte. Firstly, oxygen containing species mainly comes from the reduction of electrolytes at anode. Here, the atomic content of O on cathode side is 15.46% and 24.82% for 1 M and 3 M electrolyte, respectively. Furthermore, the anion decomposed species including S-O and N-O signals are much more abundant in the cathode with the 3 M electrolyte. These results indicate that the crosstalk phenomenon in the cell with the 3 M electrolyte is significantly more serious.
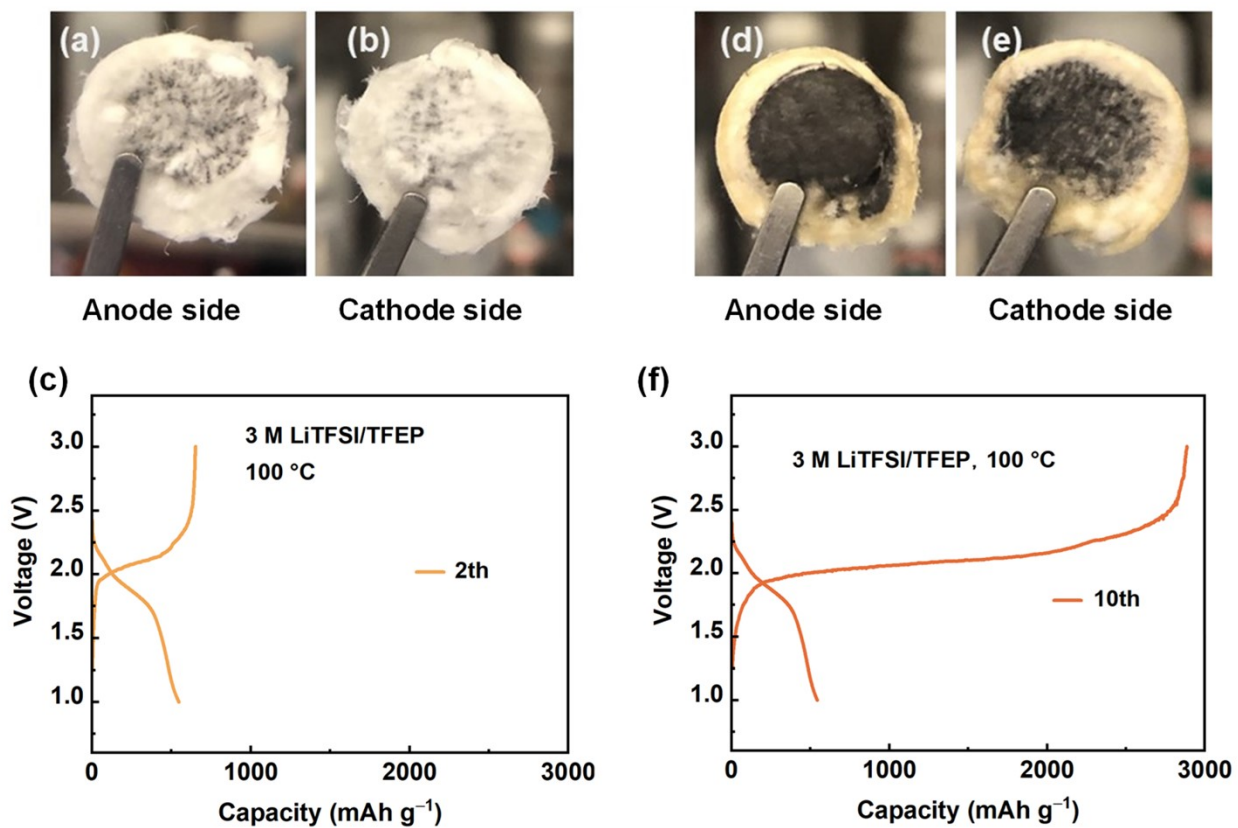
Fig. S20. Digital photographs of the glassfiber separator and the corresponding discharge-charge profile at (a-c) 2nd cycle and (d-f) 10th cycle. The Li-SPAN cells were cycled with 3 M LiTFSI/TFEP electrolyte at 100 °C. In the 2nd cycle (normal charge state), the separator facing the anode side exhibited much more obvious black products than the cathode side. After 10 cycles, the black side products began accumulating on the cathode side of the separator, coinciding with the serious cathode oxidation.
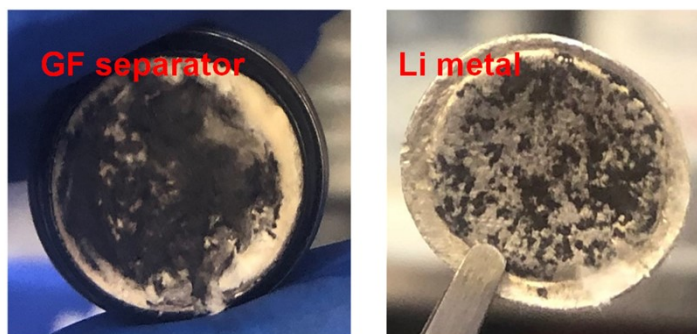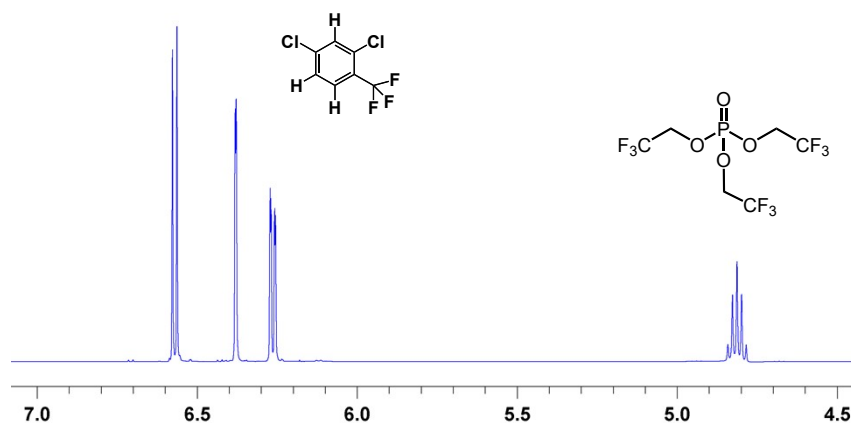
Fig. S21. Digital photographs of the glassfiber separator and the Li metal anode after cycling in 3 M LiTFSI/TFEP electrolyte at 100 °C.
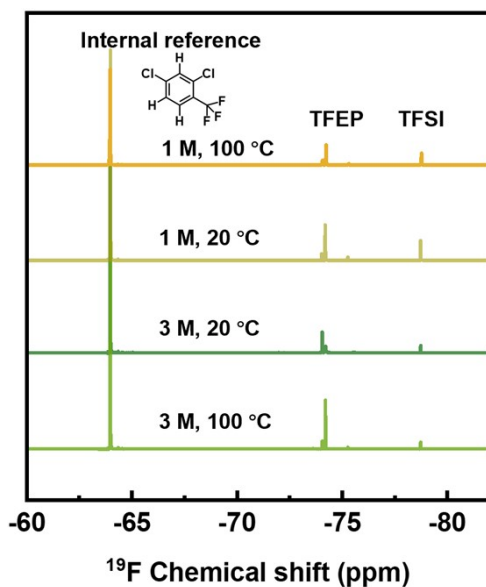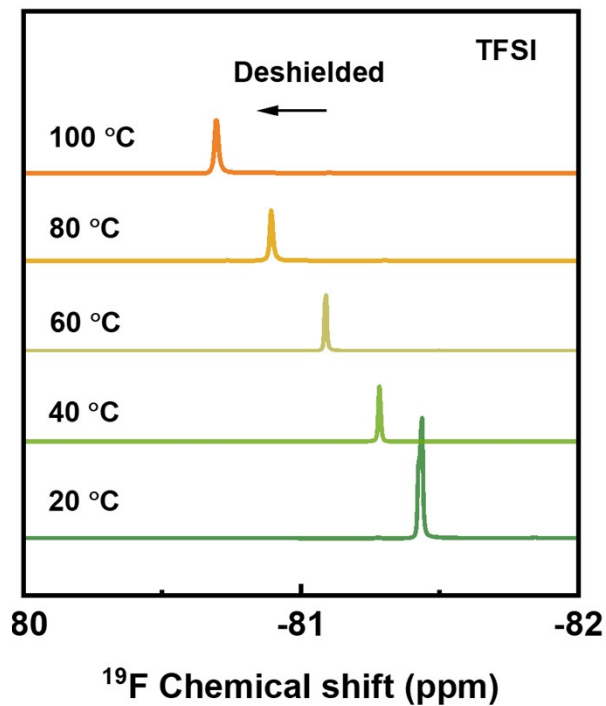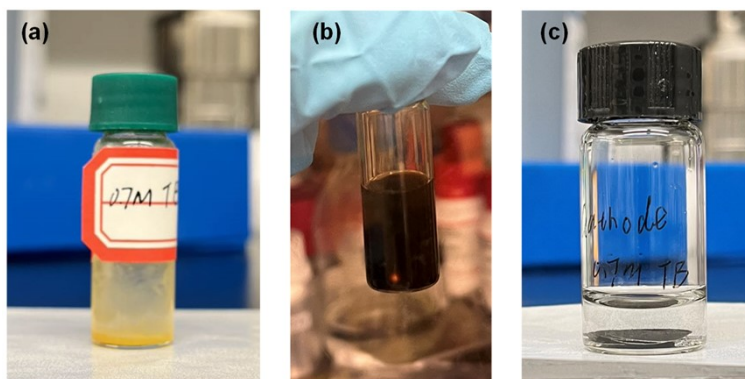
Fig. S22. ^{19}F NMR spectra of 1 M and 3 M LiTFSI/TFEP electrolytes cycled at 20 °C and 100 °C.
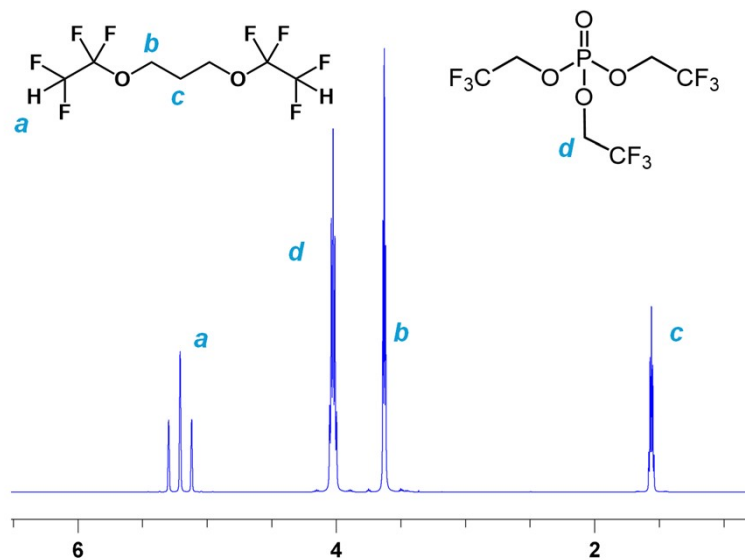

Fig. S23. ^{1}H NMR spectra of 3 M LiTFSI/TFEP electrolytes cycled at 100 °C. The three peaks at 6.2-6.6 ppm are associated with the protons of the internal reference of 2,4-dichlorobenzotrifluoride.
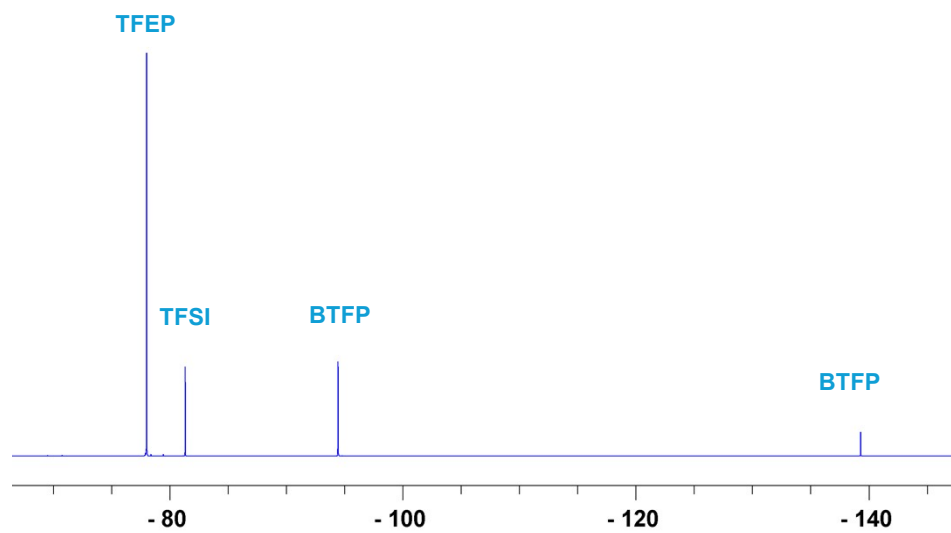
Fig. S24. ^{19}F NMR spectra of the 3 M LiTFSI/TFEP electrolytes at different temperatures.
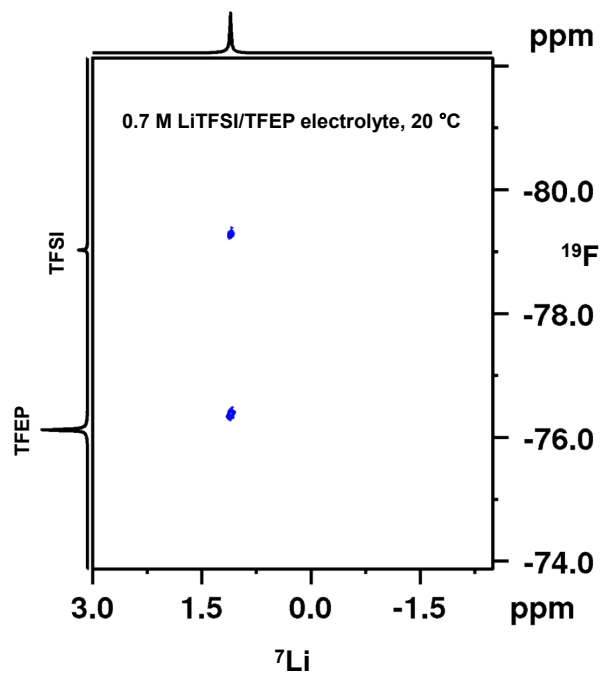

Fig. S25. Solubility test of polysulfide in (a) 0.7 M LiTFSI/TB, (b) TEGDME. (c) Cycled cathode in 0.7 M LiTFSI/TB electrolyte.
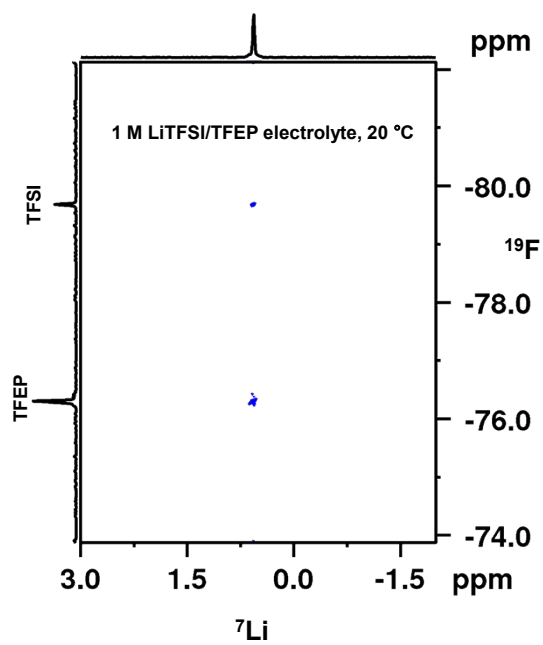
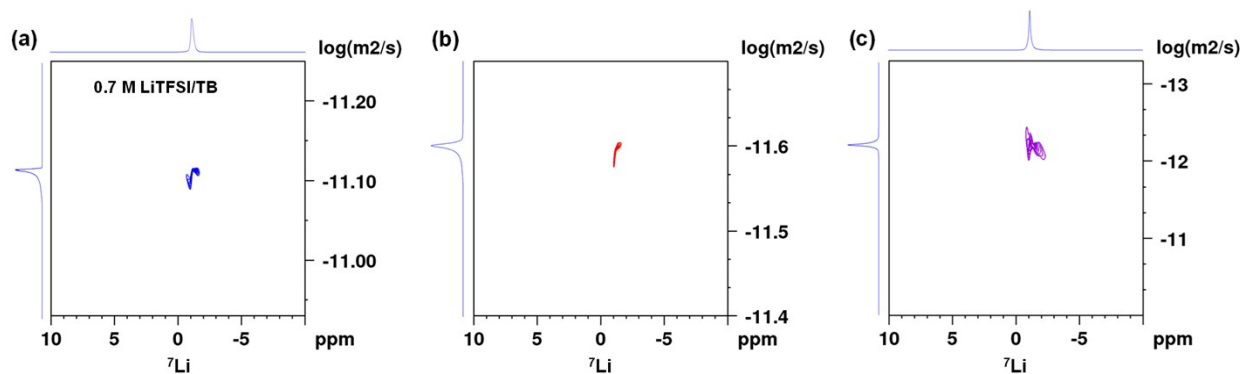**Fig. S26**. ^{1}H NMR spectrum of 0.7 M LiTFSI/TB electrolyte.

**Fig. S27**. ^{19}F NMR spectrum of 0.7 M LiTFSI/TB electrolyte.

**Fig. S28**. ^{7}Li-^{19}F HOESY spectrum for the 0.7 M LiTFSI/TB electrolyte at 20 °C.

Fig. S29. ^{7}Li-^{19}F HOESY spectrum for the 1 M LiTFSI/TFEP electrolyte at 20 °C.

Fig. S30. ^{7}Li DOSY-NMR spectra of the electrolytes for (a) 0.7 M LiTFSI/TB, (b), 1 M LiTFSI/TFEP, and (c) 3 M LiTFSI/TFEP electrolyte at 20 °C. The DOSY results show that Li^{+} diffusion coefficient is, respectively, 7.9×10^{-12}, 2.6×10^{-12}, 6.3×10^{-13} m^2 s^{-1} for the three electrolytes, following the diffusivity trend: 0.7 M LiTFSI/TB > 1 M LiTFSI/TFEP > 3 M LiTFSI/TFEP.
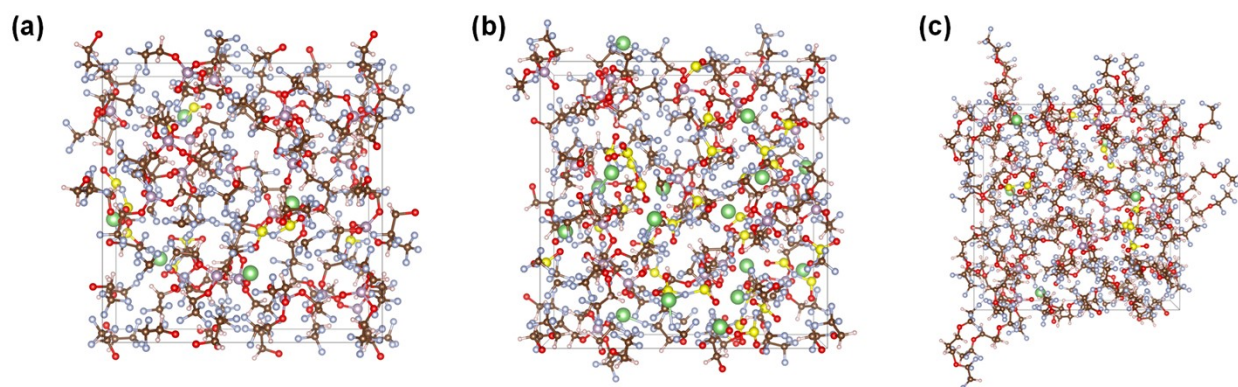
Fig. S31. Snapshoots of the AIMD simulations for the electrolytes simulated 20 °C. (a) 1 M LiTFSI/TFEP, (b) 3 M LiTFSI/TFEP, and (c) 0.7 M LiTFSI/TB.
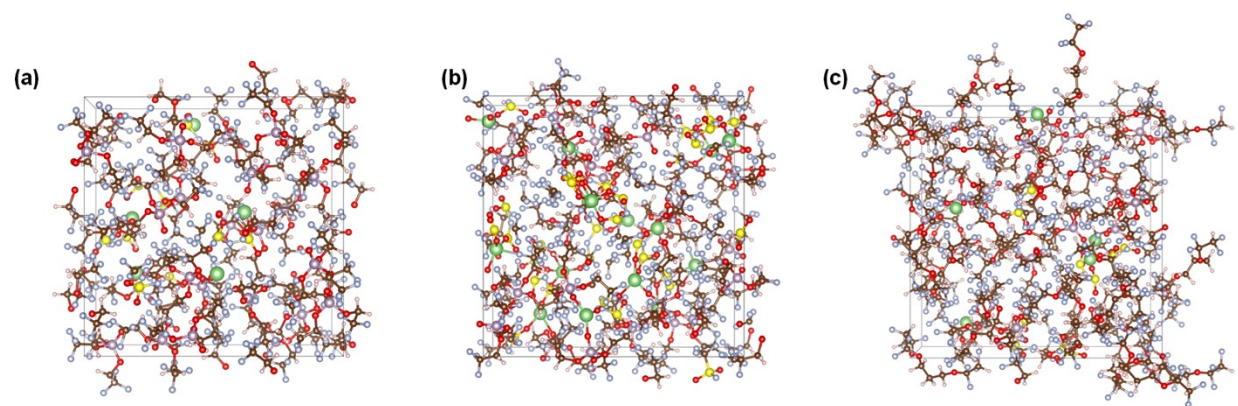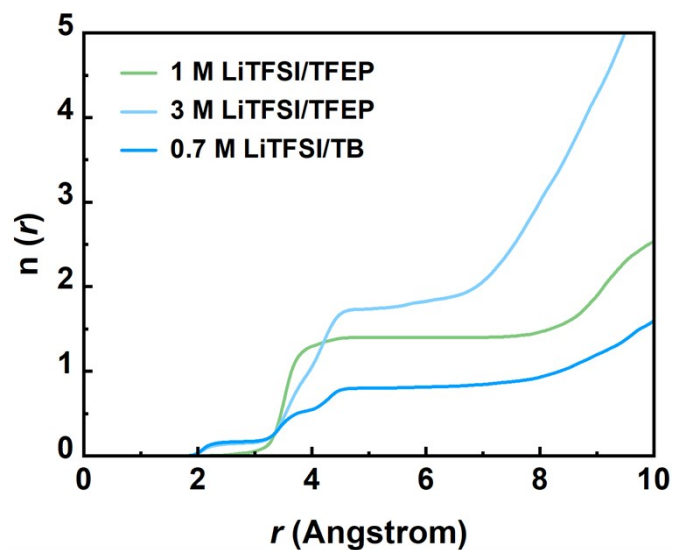

Fig. S32. Snapshoot of AIMD simulations for the electrolytes simulated 100 °C. (a) 1 M LiTFSI/TFEP, (b) 3 M LiTFSI/TFEP, and (c) 0.7 M LiTFSI/TB.

Table S 1. LUMO and HOMO levels of various solvents.

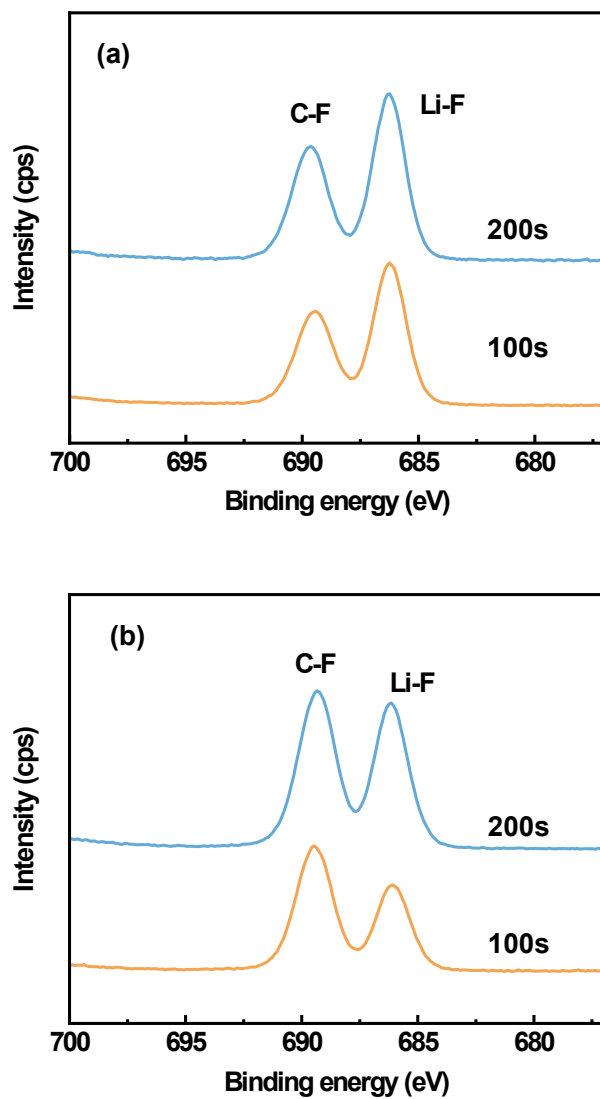| Solvents	TEGDME	TEP	TFEP	BTFP
LUMO (eV)	1.98	1.75	1.47	1.82
HOMO (eV)	-9.34	-10.12	-11.36	-11.46
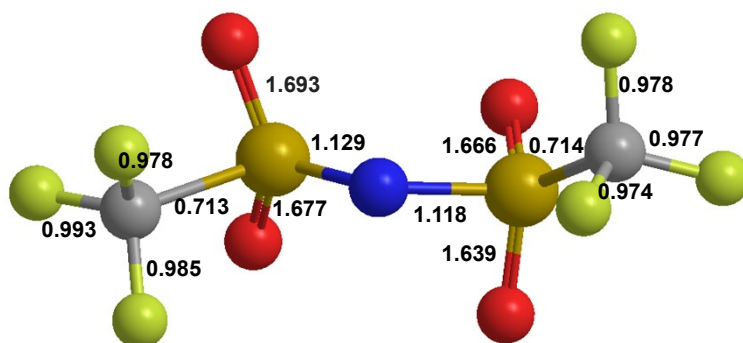
Fig. S33. Bond orders of TFSI⁻ obtained by DFT calculation. The lowest bond order is that of the S-C bond, which is 0.71.

Fig. S34. The coordination number profiles of Li–N$_{TFSI}$ for 1 M, 3 M LiTFSI/TFEP and 0.7 M LiTFSI/TB electrolytes at 20 °C.

Fig. S35. F1s XPS of Li metal anode cycled at 20 °C with (a) 0.7 M LiTFSI/TB electrolyte and (b) 1 M LiTFSI/TFEP electrolyte.
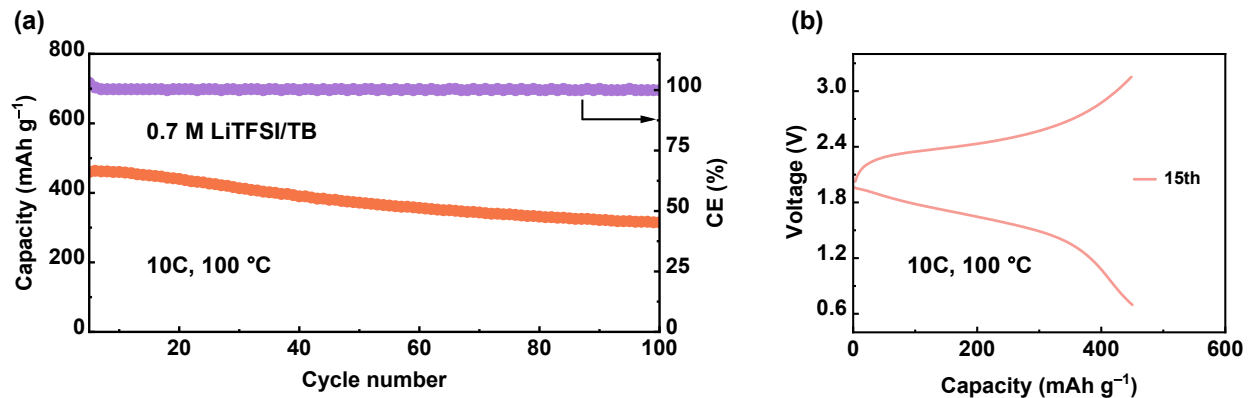
Fig. S36. (a) Cycling performance of Li-SPAN cell with 0.7 M LiTFSI/TB electrolyte at a high current density of 10C. The test temperature is 100 °C. (b) The typical discharge-charge curve at 10C under 100 °C.
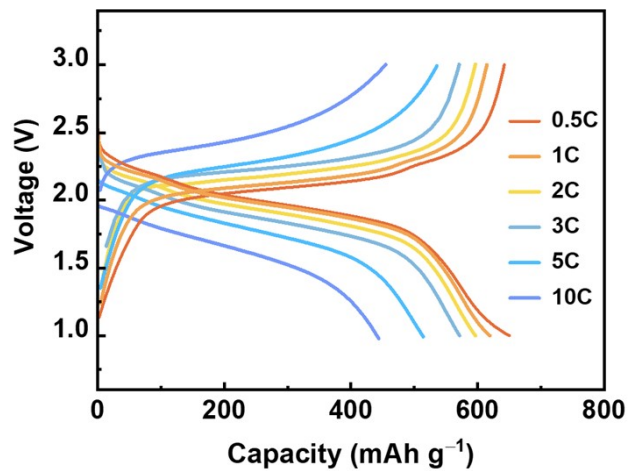
Fig. S37. (a) Discharge-charge curves of Li-SPAN cell with 0.7 M LiTFSI/TB electrolyte at different C rates. The test temperature is 100 °C.
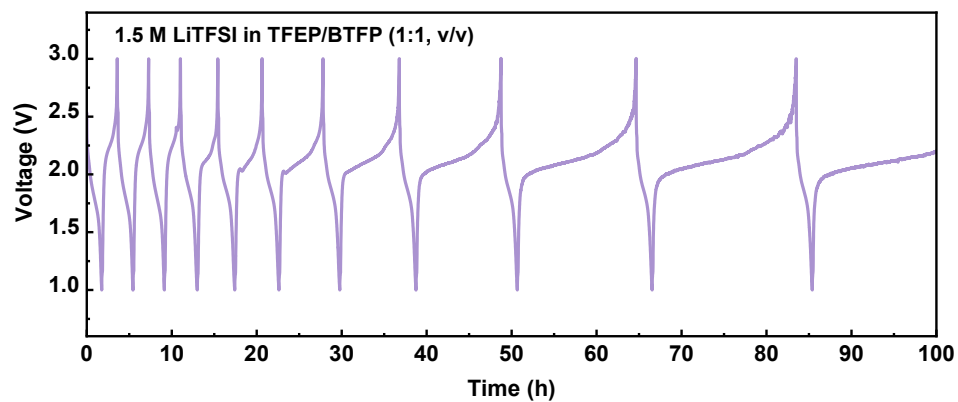
Fig. S38. (a) Discharge-charge curves of Li-SPAN cell with the 1.5 M LiTFSI in TFEP/BTFP electrolyte cycled at 100 °C. The cell with the LHCE failed at high temperatures of 100 °C, further confirming the significance of the concentration regulation for high temperature electrolytes.
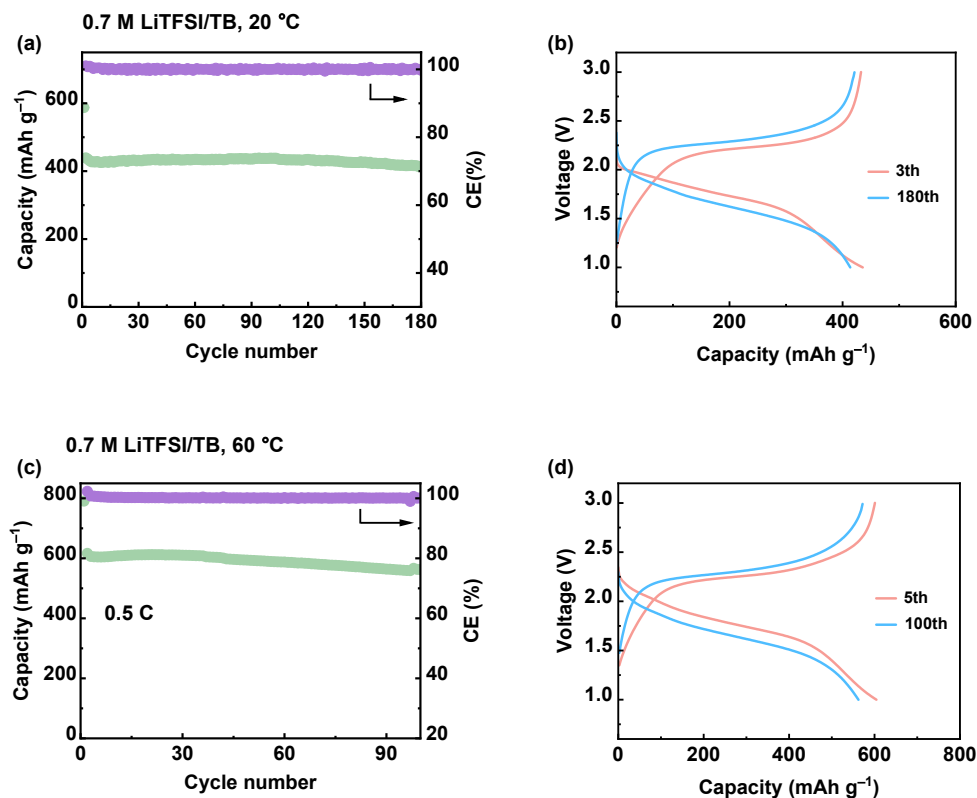
Fig. S39. The cycling performance of Li-SPAN cells with 0.7 M LiTFSI/TB electrolyte at (a-b) 20 °C and (c-d) 60 °C. C rate is 0.5C.

Table S2. Comparison of different types of batteries with the developed Li-S batteries.

Electrolytes	Cathode | Anode	Low-T Performance	Ref.
1.0 m $LiPF_6$ EC/EMC (1:2, wt) 0.5 wt% DMS	Graphite|NCM523	−10 °C@0.2 C 160 mAh g^{-1}	Guo et al.[5]
1.0 m $LiPF_6$ PC/DMC (1:1, vol) 2 vol% CMDO 3 vol% EC 5 vol% FEC	Li | MCMB	−10 °C@0.1 C ~230 mAh g^{-1} (35 cycles)	Wotango et al.[6]
1.0 m $LiPF_6$ MA/EC/DEC/EMC (3:1:1:1, vol)	MCMB|$LiNi_{0.5}Mn_{1.5}O_4$	−5 °C@0.3 C 101.7 mAh g^{-1}	Xu et al.[7]
1.0 m $LiPF_6$	Graphite | LCO	−20 °C@1 C	Won et al.[8]

EC/PC/EMC/DEC (20:5:55:20 vol%) + VC (2 wt%) + FEC (5 wt%)		~230 mAh g^{-1} 63.4% (50 cycles)	
0.8 M NaPF$_6$ in FEC/ EMC/HFE	Na | NVPOF	−20 °C@0.1 C ~115 mAh g^{-1}	Zheng et al.[9]
0.8 M THF/DOL (3:1, vol)	Na | NTP	−20 °C@0.5 C ~90 mAh g^{-1}	Zhou et al.[10]
1 M NaPF$_6$-THF/MeTHF (1:1, vol)	Na | NVP	−20 °C@0.3 C ~70 mAh g^{-1}	Wang et al.[11]
0.5 M LiTFSI + 0.3 M LiTFA + 0.2 M LiNO$_3$ in DOL/DME (85:15, vol)	Li | S	0 °C@0.1 C ~600 mAh g^{-1} (1 cycle)	Gupta et al.[12]
0.7 M LiTFSI/TB	**Li | S**	**−20 °C@0.5 C ~400 mAh g^{-1} (100 cycles)**	**This work**
		High-T Performance	
LiFSI/CsTFSI/LiTFSI (45:10:45, w%)	Li | NCA	80 °C@0.25 C ~200 mAh g^{-1}	Phan et al.[13]
1M LiFSI MTFP/FEC	Li | S	50 °C@0.1 C ~500 mAh g^{-1}	Cai et al.[14]
LiFSI: LiNO$_3$: TEGDME (1:1.2:3, molar)	Li | LFP	60 °C@0.2 C ~150 mAh g^{-1}	Chen et al.[15]
1 M NaClO3 EC/PC/FEC (47.5 : 47.5 : 5, v%)	HC | (Na$_3$V$_2$(PO4)$_2$F$_3$	55 °C@0.2 C ~120 mAh g^{-1}	Deng et al.[16]
0.7 M LiTFSI/TB	**Li | S**	**100 °C@0.5 C ~600 mAh g^{-1}**	**This work**
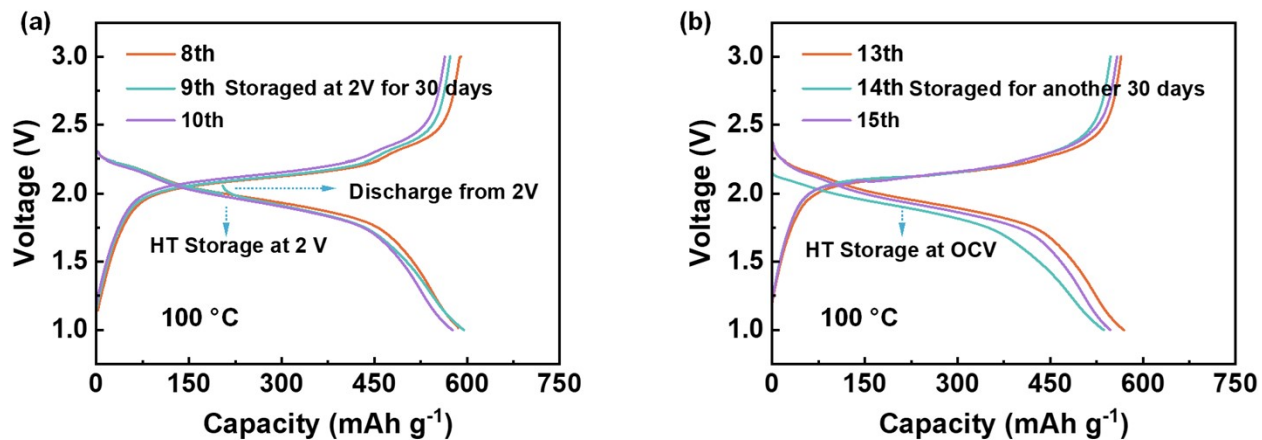
Fig. S40. Typical discharge-charge curves for the Li-SPAN cell during the high-temperature storage at 100 °C extracted from Fig. 6c. Even after an additional 30-day storage period (in a fully charged state), the cell retains a specific capacity of approximately 537 mAh g^{-1}, which is about 94.4% of the discharge capacity in the 13th cycle (before storage). Compared to the capacity in the 8th cycle, the capacity retention is approximately 90.4% after 60 days of storage at 100 °C.
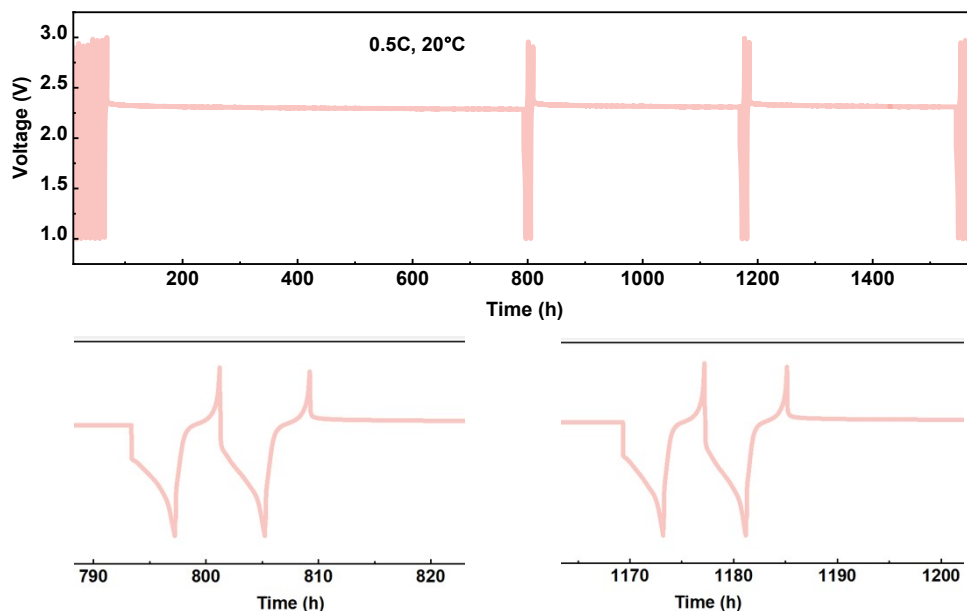
Fig. S41. (a) Storage performance of Li-SPAN cell with 0.7 M LiTFSI/TB electrolyte at 20 °C.
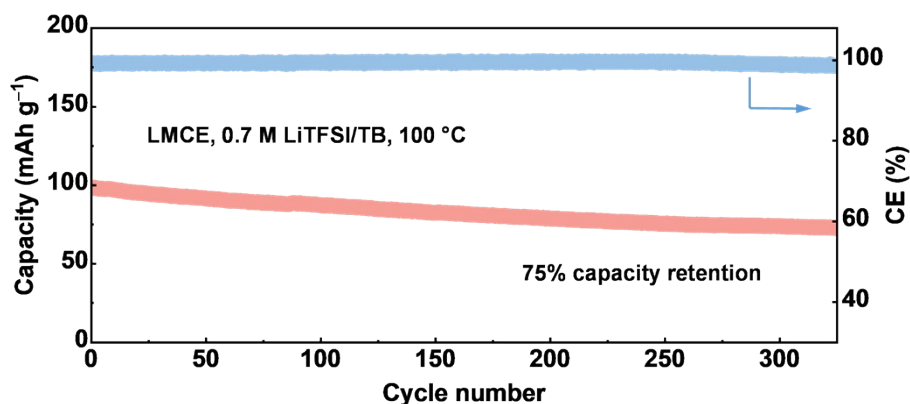
Fig. S42. Shallow discharge test at 100 °C for the Li-SPAN cell using the 0.7 M LiTFSI/TB electrolyte. The cell was cycled through discharging at a cut-off voltage of 2.1 V and then charging to 3 V. The result shows that the Li-SPAN cell can keep 75% capacity retention after 300 cycles at 100 °C, and the CE could reach over 99.5%.
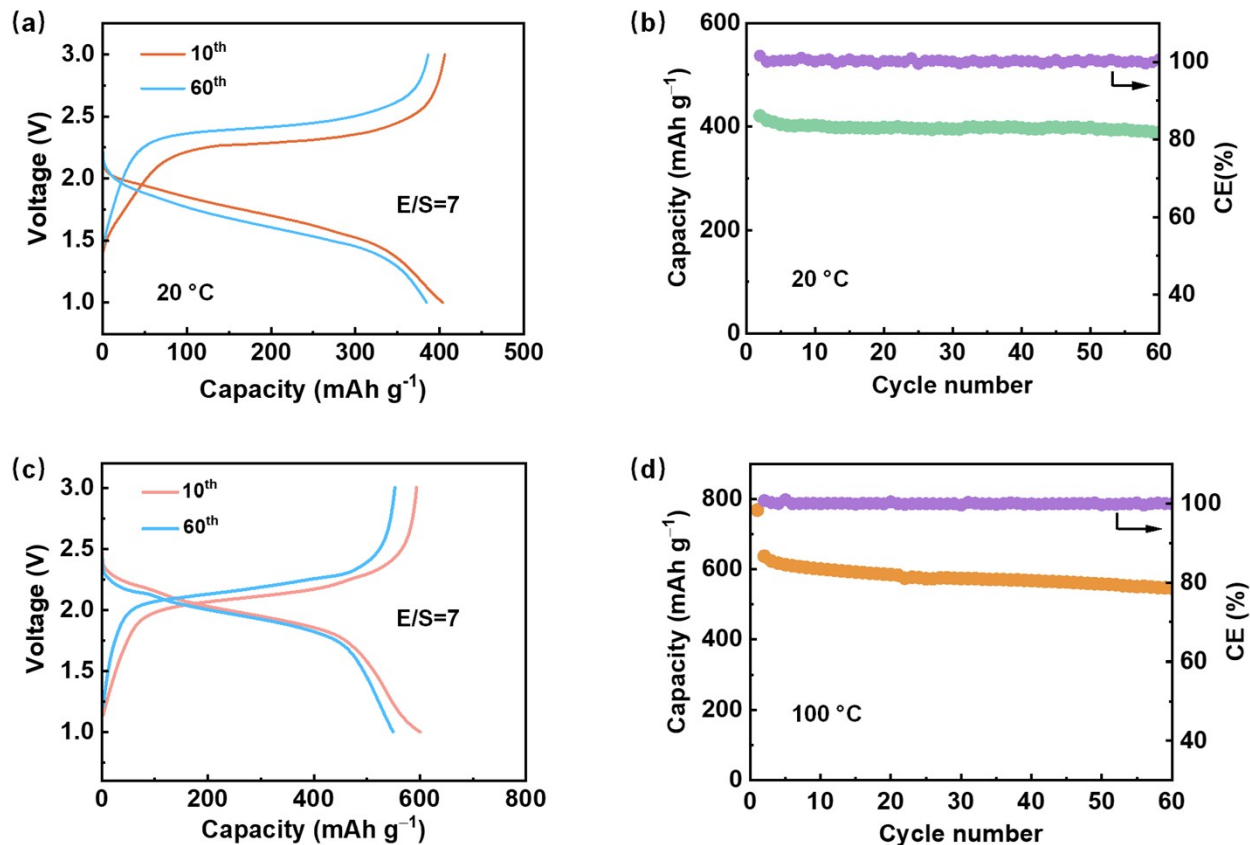
Fig. S43. Electrochemical performance of the Li-S batteries cycling at 0.5C with 0.7 M LiTFSI/TB under a lean electrolyte condition (E/S ratio: 8 μl/mg). (a, b) Discharge-charge profiles and cycling performance at 20 °C. (c, d) Discharge-charge profiles and cycling performance at 100 °C and 0.5C.

References:

1. Q. K. Zhang, S. Y. Sun, M. Y. Zhou, L. P. Hou, J. L. Liang, S. J. Yang, B. Q. Li, X. Q. Zhang and J. Q. Huang, Angew. Chem. Int. Ed. Engl., 2023, 135, e202306889.

2. Kühne, T. D., et al. Cp2k: An electronic structure and molecular dynamics software package-quickstep: efficient and accurate electronic structure calculations. J. Chem. Phys. 152, 194103 (2020).

3. Grimme, S., Antony, J., Ehrlich, S., Krieg, H. A consistent and accurate ab initio parametrization of density functional dispersion correction (DFT-D) for the 94 elements H-Pu. J. Chem. Phys. 132, 154104 (2010).

4. Gaussian 16, Revision C.02, M. J. Frisch, G. W. Trucks, H. B. Schlegel, G. E. Scuseria, M. A. Robb, J. R. Cheeseman, G. Scalmani, V. Barone, G. A. Petersson, H. Nakatsuji, X. Li, M. Caricato, A. V. Marenich, J. Bloino, B. G. Janesko, R. Gomperts, B. Mennucci, H. P. Hratchian, J. V. Ortiz, A. F. Izmaylov, J. L. Sonnenberg, D. Williams-Young, F. Ding, F. Lipparini, F. Egidi, J. Goings, B. Peng, A. Petrone, T. Henderson, D. Ranasinghe, V. G. Zakrzewski, J. Gao, N. Rega, G. Zheng, W. Liang, M. Hada, M. Ehara, K. Toyota, R. Fukuda, J. Hasegawa, M. Ishida, T. Nakajima, Y. Honda, O. Kitao, H. Nakai, T. Vreven, K. Throssell, J. A. Montgomery, Jr., J. E. Peralta, F. Ogliaro, M. J. Bearpark, J. J. Heyd, E. N. Brothers, K. N. Kudin, V. N. Staroverov, T. A. Keith, R. Kobayashi, J. Normand, K. Raghavachari, A. P. Rendell, J. C. Burant, S. S. Iyengar, J. Tomasi, M. Cossi, J. M. Millam, M. Klene, C. Adamo, R. Cammi, J. W. Ochterski, R. L. Martin, K. Morokuma, O. Farkas, J. B. Foresman, and D. J. Fox, Gaussian, Inc., Wallingford CT, 2016.

Reference:

[5] R. Guo, Y. Che, G. Lan, J. Lan, J. Li, L. Xing, K. Xu, W. Fan, L. Yu, W. Li, ACS Appl. Mater. Interfaces 2019, 11, 38285.

[6] A. S. Wotango, W. N. Su, A. M. Haregewoin, H. M. Chen, J. H. Cheng, M. H. Lin, C. H. Wang, B. J. Hwang, ACS Appl. Mater. Interfaces 2018, 10, 25252.

[7] G. Xu, S. Huang, Z. Cui, X. Du, X. Wang, D. Lu, X. Shangguan, J. Ma, P. Han, X. Zhou, G. Cui, J. Power Sources 2019, 416, 29.

[8] J. H. Won, H. S. Lee, L. Hamenu, M. Latifatu, Y. M. Lee, K. M. Kim, J. Oh, W. I. Cho, J. M. Ko, J. Ind. Eng. Chem. 2016, 37, 325.

[9] X. Zheng, Z. Gu, J. Fu, H. Wang, X. Ye, L. Huang, X. Liu, X. Wu, W. Luo, Y. Huang, Energy Environ. Sci. 2021, 14, 4936.

[10] J. Zhou, Y. Wang, J. Wang, Y. Liu, Y. Li, L. Cheng, Y. Ding, S. Dong, Q. Zhu, M. Tang, Y. Wang, Y. Bi, R. Sun, Z. Wang, H. Wang, Energy Storage Mater. 2022, 50, 47.

[11] S. Wang, X. G. Zhang, Y. Gu, S. Tang, Y. Fu, J. Am. Chem. Soc. 2024, 146, 3854.

[12] A. Gupta, A. Bhargav, J.-P. Jones, R. V. Bugga, A. Manthiram, Chem. Mater. 2020, 32, 2070.

[13] A. L. Phan, C. Jayawardana, P. M. L. Le, J. Zhang, B. Nan, W. Zhang, B. L. Lucht, S. Hou and C. Wang, Adv. Funct. Mater., 2023, 33, 2301177.

[14] G. Cai, H. Gao, M. Li, V. Gupta, J. Holoubek, T. A. Pascal, P. Liu and Z. Chen, Angew. Chem. Int. Ed. Engl., 2023, e202316786.

[15] T. Chen, Z. Jin, Y. Liu, X. Zhang, H. Wu, M. Li, W. Feng, Q. Zhang and C. Wang, Angew. Chem. Int. Ed. Engl., 2022, 61, e202207645.

[16] L. Deng, F. D. Yu, G. Sun, Y. Xia, Y. S. Jiang, Y. Q. Zheng, M. Y. Sun, L. F. Que, L. Zhao and Z. B. Wang, Angew. Chem. Int. Ed. Engl., 2022, 61, e202213416.